

# Chemiluminescent reactions of manganese with fluorine: Influence of dynamics on product energy partitioning in vibration and rotation of $\text{MnF}^*(b, c)$

Karen M. Green<sup>a)</sup> and John M. Parson

*Department of Chemistry, The Ohio State University, Columbus, Ohio 43210*

(Received 30 January 2004; accepted 20 September 2004)

Chemiluminescent exit channels of  $\text{Mn} + \text{F}_2 \rightarrow \text{MnF}^* + \text{F}$  were investigated using the molecular beam technique in a beam-gas configuration with an array detector. Two uncongested regions, corresponding to  $\text{MnF}$  transitions  $c^5\Sigma^+(b) - a^5\Sigma^+(b)$  and  $b^5\Pi_i(\text{int}) - a^5\Sigma^+(b)$  were fit for vibrational and rotational populations, which were used to develop a microscopic reaction mechanism for these chemiluminescent exit channels. In both  $\text{MnF}^*$  electronic states, significant vibrational excitation but little rotational excitation was found. Significant vibrational excitation has been attributed to early energy release as Mn loses an electron at long range to the lowest unoccupied molecular orbital on  $\text{F}_2$ . The incipient bond is strengthened as backbonding from the  $\text{F}_2^-$  to  $\text{Mn}^+$  increases the covalent character of the intermediate. Finally, no strict geometric constraints are placed on the exit channel and hence there is no significant repulsive energy release into product rotation. Our proposed mechanism exhibits dynamic control in that the course of the reaction is determined by both geometric factors and dynamic factors. © 2004 American Institute of Physics. [DOI: 10.1063/1.1814633]

## I. INTRODUCTION

Clearly there is a need for a broader base of experimental results on elementary reactions of transition metal atoms if we hope to understand how the involvement of different molecular orbitals during a reaction can provide predictions of energy partitioning into different degrees of freedom of the products.

The present study aims to extend our previous investigation into manganese reaction dynamics—this time looking at the chemiluminescent reactions with fluorine. As in previous studies, we have used the molecular beam technique in a beam-gas configuration with time-integrated spectroscopic detection. Two electronically excited product states from the  $\text{Mn} + \text{F}_2$  reaction were investigated. Dispersed radiation arising from  $\text{MnF}$   $c^5\Sigma^+ - a^5\Sigma^+$  and  $b^5\Pi_i - a^5\Sigma^+$  transitions was collected by a charge-coupled device (CCD) array detector. These spectra were then fitted to obtain vibrational and rotational state distributions of the nascent  $\text{MnF}^*$  products. Insight has been gained into the reaction mechanisms for forming these two states.

## II. REVIEW OF PREVIOUS WORK ON $\text{MnF}$

### A. Previous studies of reaction dynamics

The first investigation of chemiluminescence from  $\text{Mn} + \text{F}_2$  was carried out by Devore and Gole.<sup>1</sup> Their experimental conditions differed from those used here in two important respects: (i) they used a flow source of Mn at substantially higher temperatures that yielded Mn clusters in addition to Mn atoms, and (ii) they used a rare gas carrier at pressures

that created multicollisional pathways for forming chemiluminescent products. They interpreted the spectrum—a broad continuum punctuated in places by sharper peaks—by attributing the sharper peaks to  $\text{MnF}$  electronic transitions that had been previously observed, and the broad continuum to  $\text{Mn}_2\text{F}^*$  and  $\text{Mn}_2^*$ . A further investigation of the system under single-collision conditions seemed warranted because of uncertainty as to the primary steps in the chemiluminescence mechanism.

Aiming to identify initial reaction products, Parson and Kampf<sup>2</sup> employed an effusive metal source that minimized clustering of Mn. Less than one part in  $10^4$  of the Mn beam was estimated to be in the form of dimers. Measurements of the dependence of the chemiluminescence on the  $\text{F}_2$  pressure and the time of flight (TOF) of the Mn beam served to identify the broad continuum as arising from a process that was second order in  $\text{F}_2$ , while the sharper peaks were found to be first order in  $\text{F}_2$ . Consequently, they attributed the product of the second-order process to  $\text{MnF}_2^*$  and the product of the first-order process to  $\text{MnF}^*$ . They cited the need for further studies to investigate the details of the dynamics of the  $\text{Mn} + \text{F}_2 \rightarrow \text{MnF}^* + \text{F}$  reaction, uncomplicated by the second-order process. Consequently, the current investigation was undertaken to obtain cleaner spectra of the two most intense electronic transitions:  $\text{MnF}$   $c^5\Sigma^+ - a^5\Sigma^+$  and  $b^5\Pi_i - a^5\Sigma^+$ . Kampf and Parson reported weaker emission due to the  $d^5\Pi - a^5\Sigma^+$  and  $e^5\Sigma^+ - a^5\Sigma^+$  transitions, but there is barely enough energy to form the  $d$  and  $e$  states by the above bimolecular reaction, and so no further investigations of those transitions have been carried out. The  $\text{F}_2$  pressure was chosen to be low enough that second-order processes could be neglected. Finally, we sought to fit the observed  $c^5\Sigma^+ - a^5\Sigma^+$  and  $b^5\Pi_i - a^5\Sigma^+$  transitions by adjusting the

<sup>a)</sup>Present address: Aventis Pharmaceuticals, Tucson, AZ 85737.

TABLE I. Summary of spectroscopic constants for the quintet MnF manifold. (Values used in fitting are shown in boldface.)

	$a^5\Sigma^+$	$b^5\Pi_i$	$c^5\Sigma^+$	$d^5\Pi$	$e^5\Sigma^+$
$T_e$ (cm <sup>-1</sup> )	<b>3500</b> (±1000) <sup>b</sup> 3000(±1000) <sup>c</sup>	$T_a + 11\,751.15^d$ $T_a + 12\,000 =$ <b>15 500</b>	$T_a + 14\,493 =$ 17 993 <sup>e</sup>	$T_a + 19\,807 =$ 23 307 <sup>b</sup>	$T_a + 20\,220 =$ 23 720 <sup>b</sup>
$D_e$ (dissociation) (cm <sup>-1</sup> )	<b>32 392.2862<sup>f</sup></b>	<b>27 888.656 82<sup>f</sup></b>	<b>28 322.4496<sup>f</sup></b>		
$\omega_e$ (cm <sup>-1</sup> )	<b>645.92<sup>d</sup></b>	<b>630.54<sup>d</sup></b>	597.38 <sup>e</sup> <b>595.5<sup>g</sup></b>		
$\omega_e x_e$ (cm <sup>-1</sup> )	<b>3.22<sup>e</sup></b>	<b>3.564<sup>d</sup></b>	<b>3.15<sup>e</sup></b>		
$A_0$ (cm <sup>-1</sup> )		- <b>63.1183<sup>d</sup></b>			
$A_D$ (cm <sup>-1</sup> )		0.004 03 <sup>d</sup>			
$B$ (cm <sup>-1</sup> )	0.373 262 <sup>h,e</sup>		0.359 263 6 <sup>e</sup>	0.363 007 <sup>d</sup>	
$B_e$ (cm <sup>-1</sup> )	<b>0.374 641<sup>e</sup></b>	<b>0.373 42<sup>d</sup></b>	<b>0.360 791 5<sup>e</sup></b>		
$B_0$ (cm <sup>-1</sup> )		0.371 96 <sup>d</sup>			
$\alpha$ (cm <sup>-1</sup> )	<b>0.002 758<sup>e</sup></b>	0.002 443 <sup>d</sup> <b>0.003 025<sup>g</sup></b>	<b>0.003 055 8<sup>e</sup></b>		
$r_0$ (Å)	1.788 650 <sup>b</sup>	1.791 78 <sup>d</sup>		1.813 74 <sup>h</sup>	
$r_e$ (Å)	<b>1.7854<sup>b</sup></b> 1.785 356 <sup>e</sup>	<b>1.7883<sup>d</sup></b>	<b>1.819 300<sup>b,e</sup></b>	1.8101 <sup>b</sup>	
rot. $D$ (cm <sup>-1</sup> )	<b>5.134E-7<sup>h,e</sup></b>		<b>5.363 9E-7<sup>e</sup></b>	0 (fixed) <sup>h</sup>	
$\lambda_{\text{spin-spin}}$ (cm <sup>-1</sup> )	<b>0.413 90<sup>e</sup></b>	-1.7857 <sup>d</sup>	- <b>0.340 66<sup>e</sup></b>	-0.8886 <sup>h</sup>	
$\lambda_{\text{spin-rotation}}$ (cm <sup>-1</sup> )	- <b>0.002 053<sup>e</sup></b> -0.002 052 <sup>g</sup>	0 (fixed) <sup>d</sup>	<b>0.072 439<sup>e</sup></b>	0 (fixed) <sup>h</sup>	

<sup>a</sup>Reference 3.<sup>b</sup>Reference 10, Tables III and IV.<sup>c</sup> $T_a = T_e(a^5\Sigma^+)$ .<sup>d</sup>Reference 9, Table IIIa.<sup>e</sup>Reference 8, Table II.<sup>f</sup>Calculated assuming a Morse potential, i.e.,  $D_e = \omega_e^2/4\omega_e x_e$ .<sup>g</sup>Value used in simulation; obtained through trial and error.<sup>h</sup>Reference 7, Table II.<sup>i</sup>Reference 4.<sup>j</sup>Reference 5, Table IX.<sup>k</sup>Reference 6.<sup>l</sup>Reference 48.<sup>m</sup>Reference 49.<sup>n</sup>Reference 50.

vibrational and rotational state distributions of the electronically excited states of nascent MnF.

## B. Spectroscopic measurements

Although spectroscopic interest in MnF stretches back to the 1930s,<sup>3</sup> only two major investigations have been undertaken since then. Hayes<sup>4-6</sup> in the 1950s studied the vibrational band structure of the manganese halides and produced the first vibrational constants. Then in the 1990s Launila *et al.* reported rotational analyses of several of the systems,  $d^5\Pi-a^5\Sigma^+$ ,<sup>7</sup>  $c^5\Sigma^+-a^5\Sigma^+$ ,<sup>8</sup>  $b^5\Pi_i-a^5\Sigma^+$ ,<sup>9</sup> and  $A^7\Pi_i-X^7\Sigma^+$ , and also discussed the possible electronic configurations of all these states.<sup>10</sup> Spectroscopic constants for known states in the quintet manifold are presented in Table I. Note that  $T_e$  for the  $a^5\Sigma^+$  state is not known to better than  $\pm 1000$  cm<sup>-1</sup>, and consequently  $T_e$ 's of states in the quintet manifold are given only relative to  $T_e(a^5\Sigma^+)$ .

## III. EXPERIMENTAL APPARATUS AND PROCEDURES

Details of the apparatus and techniques employed have been previously described.<sup>11,12</sup> Oven temperatures of  $\approx 1293$

K (yielding 25 mTorr Mn) were necessary to vaporize manganese atoms from a tantalum crucible. Fluorine gas (49.9% F<sub>2</sub> in He from Air Products) was leaked into the reaction chamber by means of a needle valve so as to yield average total pressures of about 0.3 mTorr.

Light attributed to chemiluminescent products was focused on the entrance slit (physical width: 0.125 mm) of a 3/4 m Spex monochromator and was dispersed by a grating (300 or 1200 lines/mm) in first order onto a liquid nitrogen cooled, front-illuminated 1152×256 pixel CCD array (Princeton Instruments; model LN/CCD-1152-UV).

Background signals, taken with the manganese beam on but fluorine off, were acquired as five frames of 180 s each, before and after acquisition of the MnF\* spectra, which were acquired as 30 frames of 180 s each. These raw spectra were preprocessed by removing spurious peaks caused by cosmic rays and background, calibrating the wavelength scale, and correcting for detector response.<sup>13,14</sup> Additionally, when the spectral range studied was too wide to fit into one detector frame, it became necessary to join overlapping frames to produce the cumulative spectrum.<sup>15</sup>

#### IV. FITTING THE EXPERIMENTAL SPECTRA

The energies of the spectral transitions were modeled using the term-value approach, with the assumption that there are no perturbations from the other low-lying electronic states. The intensity of the light radiated by an electronically excited product in vibrational state  $v'$  and rotational state  $J'$  is given by<sup>13</sup>

$$I(v', J') \propto \frac{P(v')P_v(J')}{g_{J'}} \frac{64\pi^4\sigma^3}{3h} \times \sum_{v''} \sum_{J''} h\nu_{v', J', v'', J''} S(v', J'; v'', J''), \quad (1)$$

where  $S$  is the line strength, and  $P(v')$  and  $P_v(J')$  are the populations to be determined.

To reduce the dimensionality of the problem, populations were modeled as independent, parametric functions with the parameters determined by a nonlinear least squares fit to the experimental spectra. The analysis is Bayesian,<sup>16</sup> and so functional forms are built on the prior ( $P^\circ$ ) populations. The prior, the inverse of the density of states, is what is expected *a priori* if energy were statistically distributed in the products. The functional forms used for both the vibrational  $P(v')$  and rovibrational  $P(v', N')$  populations are given as

$$P(v') = P^\circ(v') \exp(\lambda_{vib1} f_{v'} + \lambda_{vib2} f_{v'}^2 + \lambda_{vib3} f_{v'}^3) \quad (2)$$

$$P(v', N') = P^\circ(v', N') \exp(\lambda_{rot1} g_{N', v'} + \lambda_{rot2} g_{N', v'}^2 + \lambda_{rot3} g_{N', v'}^3). \quad (3)$$

In these functions we have shifted the rotational state label from the total rotational angular momentum  $J'$  to the molecular rotational angular momentum  $N'$ , in order to simplify the form of  $P(v', J')$ . The parameters  $\lambda_i$  are Lagrangian multipliers determined by the fit.  $f_{v'}$  and  $g_{N', v'}$  refer to the fractions of energy available to the vibrational and rovibrational states, i.e.,  $f_{v'} = E_{v'}/E$ ;  $g_{N', v'} = E'_{N'}/(E - E_{v'})$ , where  $E$  is the total energy that is shared by product vibration, rotation, and translation in a given electronic state. With these distributions, the average values of the fractions of energy in product vibration  $\langle f_v \rangle$ , rotation  $\langle f_r \rangle$ , and translation  $\langle f_t \rangle$  are readily calculated using the following equations:

$$\langle f_v \rangle = \sum_{v'=0}^{v'_{\max}} P(v') \frac{E_{v'}}{E}, \quad (4)$$

$$\langle f_r \rangle = \sum_{v'=0}^{v'_{\max}} \sum_{N'=0}^{N'_{\max}(v')} P(v') P(v', N') \frac{E'_{N'}}{E}, \quad (5)$$

$$\langle f_t \rangle = 1 - \langle f_v \rangle - \langle f_r \rangle. \quad (6)$$

Since we seek the minimal functional description of the populations that will reproduce the observed spectra, we would prefer to use a four-parameter function ( $\lambda_{vib1}, \lambda_{vib2}, \lambda_{rot1}, \lambda_{rot2}$ ) rather than a six-parameter ( $\lambda_{vib1}, \lambda_{vib2}, \lambda_{vib3}; \lambda_{rot1}, \lambda_{rot2}, \lambda_{rot3}$ ) function. However the four-parameter function would be unable to represent bimodality in the distributions, which has been observed, for

example, in metal reactions with hydrocarbons.<sup>17</sup> Initially, Breckenridge thought that abstraction and insertion modes of reaction led to low  $N$  and high  $N$  components in the product rotational state distributions, respectively.<sup>17</sup> However, Liu *et al.*,<sup>18</sup> demonstrated that the bimodal rotational distributions were independent of temperature, and demonstrated that excitation in different vibrational modes of a short-lived reaction complex could produce varying amounts of rotational and vibrational excitation in the product molecules due to distinctly different forces acting during the separation. Work on these systems was extended more recently by Wong *et al.*<sup>19</sup> who noted, for a range of magnesium-alkane reactions that entrance channel forces determine the vibrational energy partitioning while it is the exit channel forces that determine the rotational energy partitioning. Experimental and theoretical photodissociation studies<sup>20–23</sup> uphold these results. Ideally, the best-fit rotational state distribution should be determined for each vibrational product state populated in order to gain the most dynamical insight, but it was impractical to do that here because of extensive overlap of rotational bands belonging to different vibrational states.

#### A. Line strengths

We assume complete separability of the wave function which implies that the transition moment may be factored into a product of the electronic transition moment, the vibrational band strength (Franck-Condon factor), and the rotational line strength. Since the procedures for calculating the vibrational band strengths and electronic transition moments were treated as in our previous papers, we comment here only on the rotational line strengths.

Rotational line strengths were calculated using the analytical expressions given in the literature.<sup>24–29</sup> (An explanation of the quantum number convention used in Kovács' text is given elsewhere.<sup>12</sup>) Although for the  $c^5\Sigma^+ - a^5\Sigma^+$  transition there is no question that both states can be described as pure Hund's case (b), this is not the case for the  $b^5\Pi_i - a^5\Sigma^+$  transition as attested by poor initial attempts at fitting this region using a  $^5\Pi_i(a) - ^5\Sigma^+(b)$  representation of the transition. Rather, the  $b^5\Pi_i$  state is seen to be better described as an intermediate case between Hund's cases (a) and (b).

Finally, Kovács' equations, which are given explicitly only for the normal  $^5\Pi_i - ^5\Sigma^+$  transition, were adapted for the inverted one ( $^5\Pi_i - ^5\Sigma^+$ ). Since the changes needed in his equations were not immediately obvious, we describe the two necessary modifications. First, the numbers in the rotational branch symbols that correspond to the  $\Pi$  state were relabeled, according to the pattern, 1→5, 2→4, ... [An example of this for the  $^5\Pi_i - ^5\Sigma^+$  branch symbols is  $R_2 \rightarrow R_{42}$ ,  $P_{R_{35}} \rightarrow P_{R_{35}}$ . Note  $P_{R_{35}}$  corresponds to a transition from  $F_3$  to  $F_5$  with  $\Delta N = -1(P)$  and  $\Delta J = +1(R)$ .] More details can be found elsewhere.<sup>30–32,24,25,33,12</sup> Second, the equations themselves were modified. Specifically, for the original equations to remain valid for both normal and inverted terms,  $Y$  and  $\Lambda$  were replaced by their absolute values. Rotational transitions are shown in Figs. 1 and 2 for the relevant transitions.

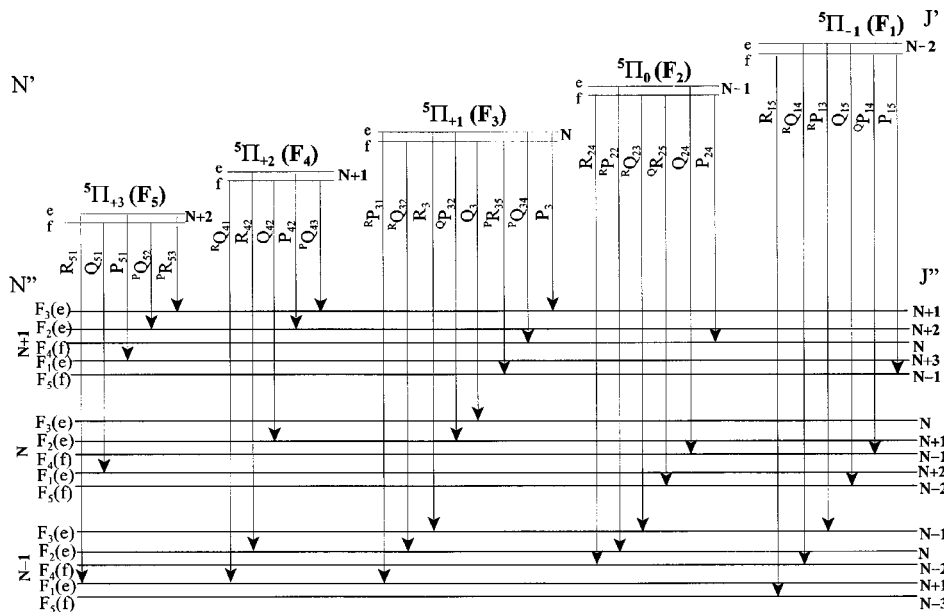


FIG. 1. Rotational transitions for  ${}^5\Pi_i(a)-{}^5\Sigma^+(b)$ .

**B. Energy constraints**

The fit is constrained by the initial energy conditions, which are listed in Table II. The values given correspond to the most probable initial conditions. To address the spread in the initial conditions, we added  $2150\text{ cm}^{-1}$  to the nominal total energy available. This amount was chosen so as to allow population of the highest vibrational product states that were observed to radiate. Table III gives the energy available for sharing among vibrational, rotational, and translational degrees of freedom of the products when the *b* or *c* state is formed.

**V. EXPERIMENTAL RESULTS**

**A. Spectra**

The spectrum for the  $\text{MnF } c\text{ } {}^5\Sigma^+ - a\text{ } {}^5\Sigma^+$  transition taken at an effective bandwidth of  $5.5\text{ \AA}$  is displayed in Fig. 3, and

the spectrum for the  $\text{MnF } b\text{ } {}^5\Pi_i - a\text{ } {}^5\Sigma^+$  transition taken at an effective bandwidth of  $1.1\text{ \AA}$  is shown in Fig. 4. The labels “best fit,” “fit,” and “prior” that are used to label the  $c\text{ } {}^5\Sigma^+ - a\text{ } {}^5\Sigma^+$  spectrum will be explained later. As mentioned earlier, we were not able to fit the  $b\text{ } {}^5\Pi_i - a\text{ } {}^5\Sigma^+$  transition when we assumed the *b* state was pure Hund’s case (a)—it was possible only after we implemented the intermediate (a)-(b) Hund’s case for the rotational line positions and strengths. Also in this transition, modifying the spectroscopic constant  $\alpha_e$  for  $b\text{ } {}^5\Pi_i$ —using a value of  $0.003\,025\text{ cm}^{-1}$  that was obtained through iterative trial and error in place of the literature value of  $0.002\,443\text{ cm}^{-1}$ —vastly improved the fit.

Although we have obtained best-fit populations from our experimental data, we wish to stress that they are dependent on both experimental accuracy—primarily limited by correction for the background signal and the finite resolution—and theoretical accuracy of the model used. Consequently, when

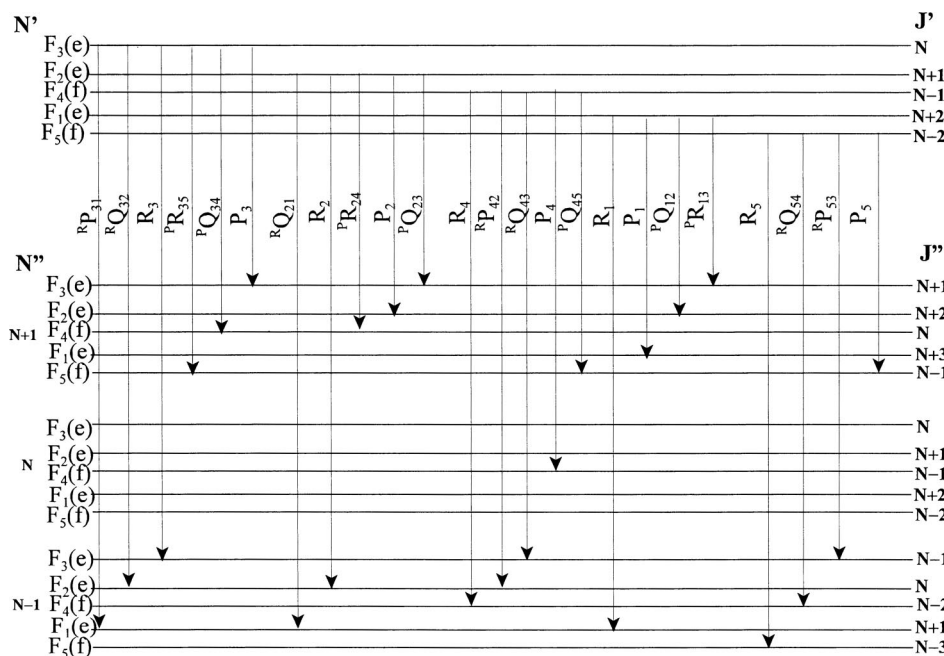


FIG. 2. Rotational transitions for  ${}^5\Sigma^+(b)-{}^5\Sigma^+(b)$ .

TABLE II. Energy constraints on the spectral fit of  $\text{Mn} + \text{F}_2$ . The subscripts *int*, *trans*, *rot*, and *vib*, respectively, refer to internal, translational, rotational, and vibrational. Energy available for the chemiluminescent product is computed from the sum of the reaction exothermicity and the reactants' relative translational and internal energies.

Parameter	Values		
	[eV]	( $\text{cm}^{-1}$ )	(K)
$D_0^0(\text{F}-\text{F})^a$	1.6		
$D_0^0(X^7\Sigma^+ \text{MnF})^b$	4.388		
$ \Delta E $ (exothermicity)	2.788		
$T_{\text{fluorine}}$ (assumed)			293
$T_{\text{Mn}}$			1293
$T_{\text{effective:Mn fluorine}}^c$			702
$E_{\text{trans}}^e$		732	
$E_{\text{rot,fluorine}}^d$		203.643 79	
$E_{\text{vib,fluorine}}^e$		0	
$E_{\text{int}}$		203.643 79	

<sup>a</sup>Reference 3.

<sup>b</sup>Reference 51.

<sup>c</sup>The relative translational energy of the reactants was calculated as  $E_{\text{trans}} = \frac{3}{2}k_B T_{\text{effective}}$ , where  $T_{\text{effective}} = m_{\text{Mn}}T_{\text{F}_2} + m_{\text{F}_2}T_{\text{Mn}}/m_{\text{total}}$ .

<sup>d</sup>The rotational energy of the reactants here was calculated as  $E_{\text{rot,fluorine}} = k_B T_{\text{fluorine}}$ .

<sup>e</sup>The vibrational energy of fluorine is assigned this zero value because at the fluorine temperature the ambient energy is  $203.635 \text{ cm}^{-1}$  ( $k_B T_{\text{fluorine}}$ ) and this is significantly less than the energy required to excite vibration in fluorine ( $916.64 \text{ cm}^{-1}$ ).

trying to determine why we did not achieve a very good fit, we need to examine both these sources of error. A close examination of the spectral fits indicates how the best-fit spectra systematically deviate from the experimental ones. For example, for the  $c^5\Sigma^+ - a^5\Sigma^+$  transition, the peaks are relatively well aligned, signifying that the energies are well described by the theoretical model. On the other hand, although the general envelope appears relatively close to the experiment, the intensities are off to some extent. We believe that the deviation is caused by an experimental artifact. Uncertainty in the correction for the background signal can create a corresponding uncertainty in the relative heights of the spectral maxima and minima. For example, if insufficient background signal is removed from the experimental spectrum, then the fitting routine is forced to make the peaks higher than observed so as to keep a decent fit to the lower parts of the spectrum.

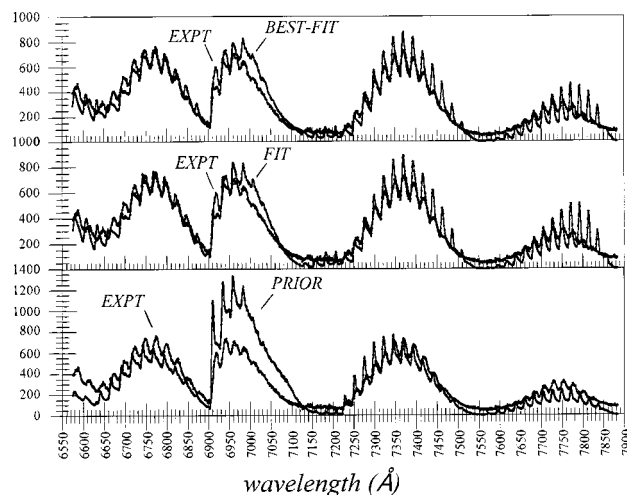


FIG. 3. Comparison of  $\text{MnF } c^5\Sigma^+ - a^5\Sigma^+$  spectra—experiment, best-fit, fit, and prior.

## B. Populations and surprisals

The vibrational populations for the *c* state are shown in Fig. 5, and for the *b* state in Fig. 6. The rotational populations for the *c* state are shown in Fig. 7, and for the *b* state in Fig. 8. First, we comment on the functional forms used to describe the populations, and then discuss the vibrational populations and finally the rotational populations. Although some conclusions concerning the populations will be discussed in this section, the implications for the mechanism will be presented later.

For fitting the *c*-*a* transition, the fully optimized four parameters were used as the starting point in both the best fit and also the fit spectra shown in Fig. 3. The best fit was obtained by a full optimization of the six parameters; whereas, the fit was obtained by fixing the rotational parameters to the two-parameter solution but fully optimizing the three vibrational parameters. The best fit produced the lower observed sum of squares of deviations, an  $L^2$  value of 2598 vs 2684, although the fit produced the better Pearson correlation, an  $R^2$  value of 0.910 vs 0.906. The vibrational populations for the  $c^5\Sigma^+$  state for both the fit and best-fit cases are compared in Fig. 5. Since they are nearly the same, apparently only two of the three vibrational parameters are actually needed to describe the vibrational distribution. Both the fit and best-fit vibrational populations differ markedly

TABLE III. Summary of results for energy partitioning in the *b* and *c* states of  $\text{MnF}$  using different fitting procedures. See text for definitions.

State	$b^5\Pi_i$	$b^5\Pi_i$	$b^5\Pi_i$	$c^5\Sigma^+$	$c^5\Sigma^+$	$c^5\Sigma^+$
Fit specifics	Six-parameter, var. $\alpha_e$	Six-parameter, lit. $\alpha_e$	Prior	Five-parameter	Six-parameter	Prior
$L^2$	5137	7220	17 268	2684	2598	5933
$R^2$	0.914	0.839	0.239	0.910	0.906	0.699
$E_{\text{available}}$ (eV)	1.25	1.25	1.25	0.94	0.94	0.94
$\langle f_v \rangle$	0.514	0.491	0.280	0.395	0.386	0.270
$\langle f_r \rangle$	0.128	0.144	0.288	0.220	0.190	0.292
$\langle f_i \rangle$	0.358	0.365	0.432	0.385	0.424	0.438

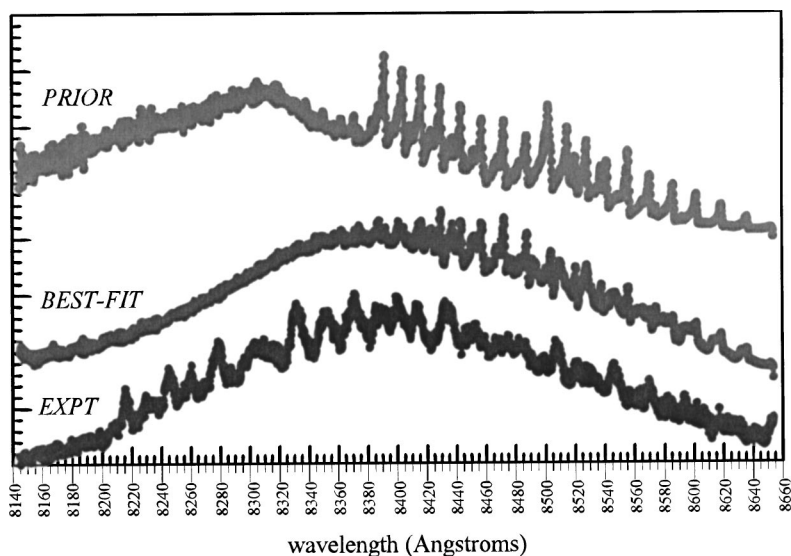
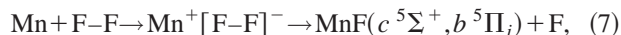


FIG. 4. Comparison of MnF  $b^5\Pi_i - a^5\Sigma^+$  spectra—experiment, best-fit, and prior.

from the prior populations. We can conclude that the experimental spectrum displays significantly less population than expected for low vibrational states, and considerably more than expected at moderate to higher vibrational states. We see even higher than expected vibrational excitation in the  $b^5\Pi_i$  state, as shown in Fig. 6. This vibrational excitation is not unexpected in MnF as the product is considered to be highly ionic, suggesting that the electron transfer could occur at long range. To explore the implications of a long-range electron transfer, we use Magee's equation<sup>34</sup> to estimate the crossing radius at the electron jump. Using the first ionization energy for Mn of 7.43 eV,<sup>35,36</sup> and the most recently determined electron affinity value for F<sub>2</sub> of 3.01 eV,<sup>37</sup> we obtain a value of 3.26 Å for the crossing radius of the lowest covalent surface (Mn+F<sub>2</sub>) with the lowest ionic surface (Mn<sup>+</sup>+F<sub>2</sub><sup>-</sup>). This is a relatively large distance compared to the equilibrium bond length of MnF (see Table I). The reaction then could be represented as



and an early release of the Coulombic attraction of Mn<sup>+</sup> and F<sup>-</sup> can channel energy efficiently into vibration of MnF.

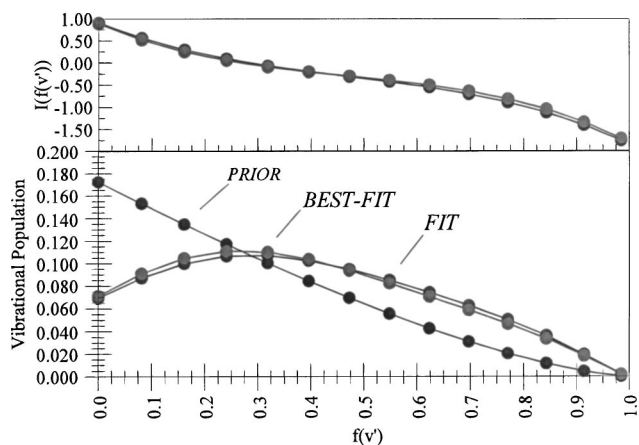


FIG. 5. Vibrational populations and surprisals for MnF  $c^5\Sigma^+$ .

Thus, we believe that the considerable vibrational excitation that appears in the product is determined primarily by the entrance channel forces.

Overall, for both the  $c-a$  and  $b-a$  transitions, we did not observe significant rotational excitation (see Figs. 7 and 8). The distributions were colder than the prior distributions, and were much colder than the product MnO rotational distribution that was found for the  $\text{Mn} + \text{O}_3 \rightarrow \text{MnO}(A^6\Sigma^+) + \text{O}_2$  reaction.<sup>38</sup> Table III compares the average fractions of available energy that appear in vibration, rotation, and translation for the  $b$  and  $c$  states. Notice that these values do not change much with the somewhat arbitrary choice of a fitting procedure. The rotational distribution for  $v'=0$  observed in the  $b$  state was noticeably colder than that found for the  $c$  state. The peak in the  $b$  rotational distribution is at a lower value of  $g_{N',v'=0}$ , and this is reflected in a lower value of  $\langle f_r \rangle$ . There is possibly a slight bimodality in the rotational distributions observed for both states with the major component lying at low  $N'$  and a much smaller minor component possibly formed at high  $N'$ .

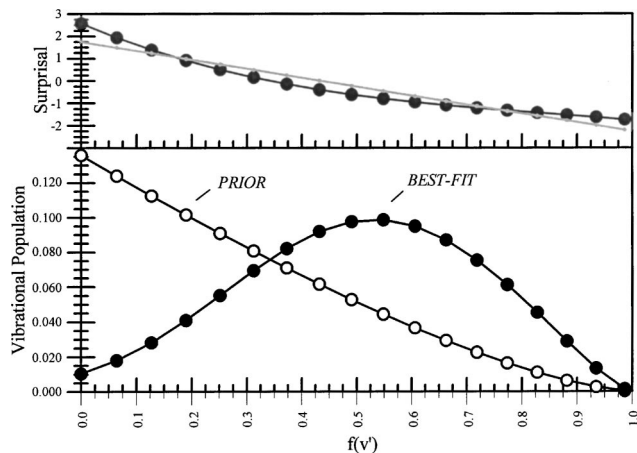
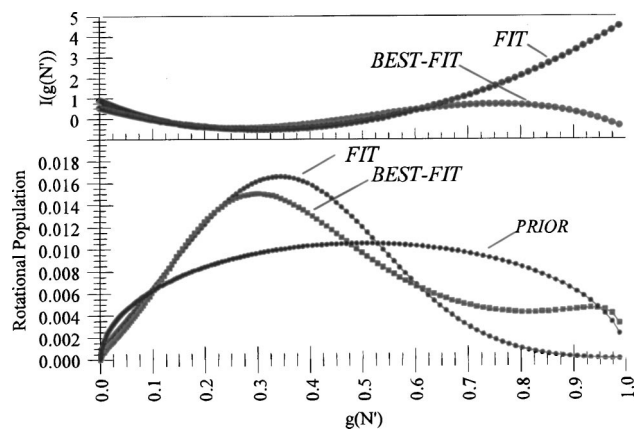


FIG. 6. Vibrational populations and surprisals for MnF  $b^5\Pi_i$ .

FIG. 7. Rotational populations and surprisals for  $v' = 0$  of  $\text{MnF } c^5\Sigma^+$ .

## VI. ELECTRONIC STATES OF MnF

In order to explore the pathways leading to the observed electronically excited states of MnF, it is essential to identify the leading molecular orbital configurations of those states. Previous assignments of the configurations, however, are puzzling and appear to be based on an inappropriate analogy with states of MnH. It will be shown below that the corresponding states of CrF and MnO provide a more reasonable interpretation of the observed visible transitions of MnF.

In order to understand better the electronic states involved in the  $\text{Mn} + \text{F}_2 \rightarrow \text{MnF}^* + \text{F}$  reaction, we first seek to build a molecular orbital diagram for the MnF product. In the case of MnF lack of computational studies handicapped the spectroscopists in their investigations. Resorting to an analogy to MnH, whose electronic structure is better understood, does not appear appropriate since the charge on the H could be either positive or negative.<sup>39</sup> A better analogy would be to a case with more clearly defined polarity—that of a transition metal halide or oxide.

For another study,<sup>15</sup> we had created a CrF diagram by using different combinations of orbital interactions and application of simple rules<sup>40–42</sup> of MO theory. Since the metal orbitals can hybridize in different ways, with no *a priori* way to decide which are the most likely combinations, only the

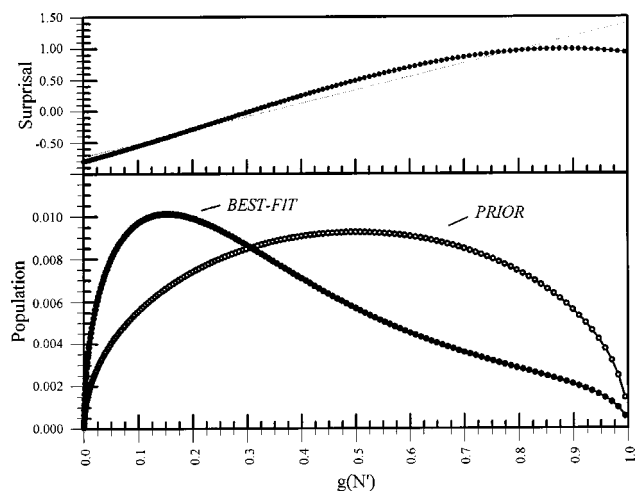
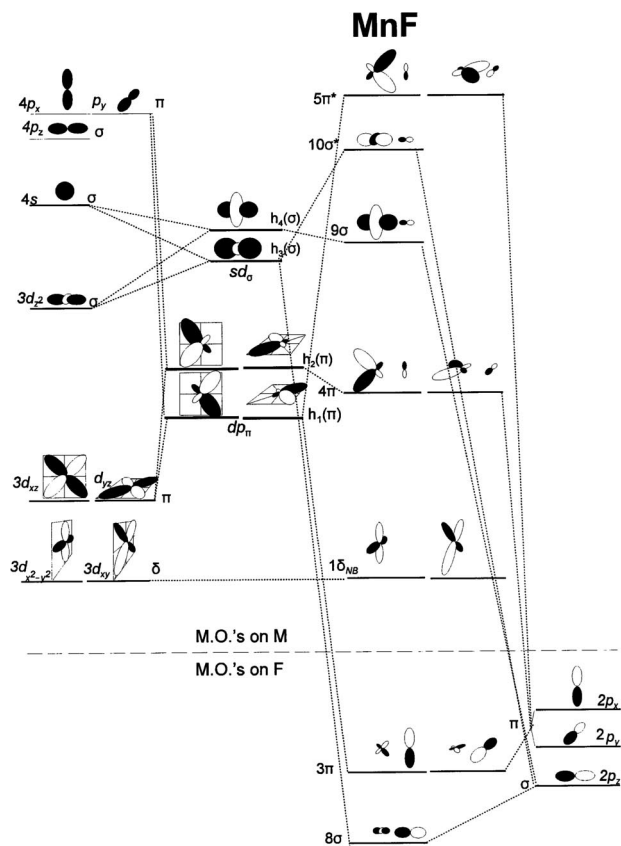
FIG. 8. Rotational populations and surprisals for  $v' = 0$  of  $\text{MnF } b^5\Pi_i$ .

FIG. 9. Molecular orbital diagram for MnF.

simplest pairwise hybridization schemes were generated. These schemes were then used to build up molecular orbitals of CrF which were visually compared to the CrF orbital amplitude plots given in recent computational investigations.<sup>43,44</sup> The successful scheme (shown in Fig. 9) was the one that produced molecular orbitals that were a topological match to the amplitude plots.

The aim here is to apply this diagram to describe the leading electronic configurations of the low-lying states of MnF. Although these states are not well described by a single configuration, the single-configuration representations can provide qualitative insight into the nature of the two MnF transitions of interest here. As indicated earlier, this will require the current literature assignments to be revised so that transitions make physical sense.

Launila *et al.*<sup>10</sup> give the assignments shown in Fig. 10 for the leading configurations of the lowest-lying observed electronic states of MnF. These assignments have two major flaws: emission of radiation in the *b-a* and *c-a* transitions appears to be associated with promoting an electron to *higher* molecular orbitals, and neither molecular orbital change is expected to give rise to an electric-dipole allowed transition. With their assignment of  $8\sigma^2 3\pi^4 1\delta^2 4\pi^2 9\sigma^2$  for  $c^5\Sigma^+$ , the  $c^5\Sigma^+ \rightarrow a^5\Sigma^+$  emission would have to involve unpairing and transferring an electron in the  $9\sigma$  MO to the  $10\sigma^*$  MO. Likewise, with the assignment of  $8\sigma^2 3\pi^4 1\delta^2 4\pi^3 9\sigma^1$  for  $b^5\Pi_i$ , the  $b^5\Pi_i \rightarrow a^5\Sigma^+$  emission would have to involve unpairing and transferring an electron in the  $4\pi$  MO to the  $10\sigma^*$  MO. Clearly, one would

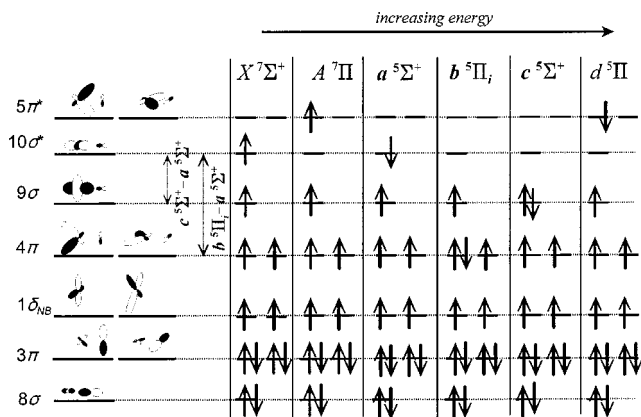


FIG. 10. Single-configuration representations of the low-lying electronic states of MnF, as assigned in the current spectroscopic literature.

expect the antibonding  $10\sigma^*$  MO to lie higher in energy than the  $9\sigma$  and  $4\pi$  MOs.

Another problem with the  $c\ 5\Sigma^+$  assignment is that the  $10\sigma^*$  and  $9\sigma$  MOs are both centered largely on Mn, with  $10\sigma^*$  arising mainly from the Mn  $3d_\sigma$  atomic orbital and  $9\sigma$  mainly from the Mn  $4s$  atomic orbital. This would imply that a  $3d_\sigma \rightarrow 4s$  atomic transition can be used to estimate the strength of this MnF electronic transition, but such a transition is electric-dipole forbidden. Our observation of intense  $c \rightarrow a$  emission suggests a radiative lifetime less than the time interval of  $\sim 10^{-5}$  s that is needed to escape from the observation zone. The only way to explain an intense transition with these MO assignments would be to suppose that the ligand field of the  $F^-$  strongly distorts the  $Mn^+$  orbitals, but that would be inconsistent with the fact that  $Mn^+$  is in a high spin state. Further, if the  $c \rightarrow a$  transition were metal centered, then one would expect a nearly vertical transition. That would be inconsistent with the substantial lengthening of  $r_e$  and decrease in  $\omega_e$  observed for the  $c$  state compared to the  $a$  state.

To form the bond in the  $c\ 5\Sigma^+$  state, we expect that one electron transfers from Mn to F ( $Mn \rightarrow Mn^+$ )—a charge transfer transition (and so expected to have a large transition moment). By symmetry arguments, this electron must come from one of the Mn  $sd$  hybrids and must transfer to the  $F\ 2p_\sigma$ . These hybrids correlate to three MnF molecular  $\sigma$  orbitals of interest— $8\sigma$ ,  $9\sigma$ , and  $10\sigma^*$ .  $9\sigma$  and  $10\sigma^*$  are centered on the metal while only  $8\sigma$  is centered on the ligand. This implies then that the only MO that could conceivably receive the Mn-donated electron is  $8\sigma$ , and so we reassign the  $c\ 5\Sigma^+$  state as  $8\sigma^1 3\pi^4 1\delta^2 4\pi^2 9\sigma^2 10\sigma^{*1}$  as shown in Fig. 11. This assignment means that  $c\ 5\Sigma^+ \rightarrow a\ 5\Sigma^+$  corresponds to a charge transfer,  $9\sigma \rightarrow 8\sigma$ .

We encounter the same type of difficulty with the assignment of Launila *et al.* of the  $b\ 5\Pi_i$  state MO configuration as  $8\sigma^2 3\pi^4 1\delta^2 4\pi^3 9\sigma^1$ . The  $4\pi \rightarrow 10\sigma^*$  transition would be metal centered and would be weak since the  $4\pi$  MO is mainly  $3d_\pi$  and the  $10\sigma^*$  MO is mainly  $3d_\sigma$ . Again that is inconsistent with our observation of strong  $b \rightarrow a$  emission. Since the MnF bond is thought to be best described as  $Mn^+F^-$ , the  $b\ 5\Pi_i$  bond will require one electron transfer from Mn to F—again, a charge transfer transition and hence

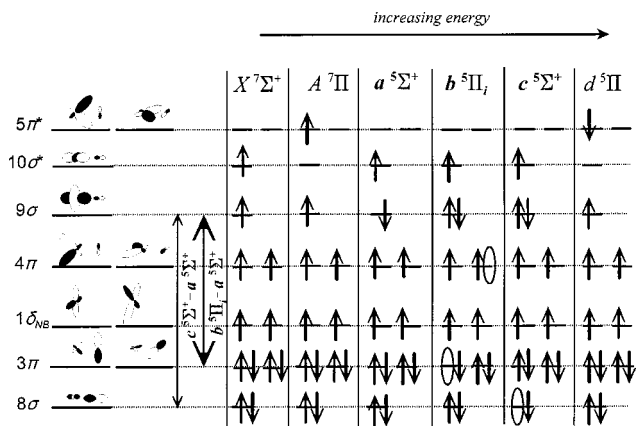


FIG. 11. Revised assignments of low-lying single-configuration representations of MnF.

expected to be intense. By symmetry arguments, this electron must come from one of the Mn  $pd_\pi$  hybrids and must transfer to the  $F\ 2p_\pi$ . These correlate to three molecular  $\pi$  orbitals of interest— $3\pi$ ,  $4\pi$ , and  $5\pi^*$ .  $4\pi$  and  $5\pi^*$  are centered on the metal while only  $3\pi$  is centered on the ligand. This implies then that the only MO that could conceivably receive the Mn-donated electron is  $3\pi$ , and so we reassign the  $b\ 5\Pi_i$  state as  $8\sigma^2 3\pi^3 1\delta^2 4\pi^2 9\sigma^2 10\sigma^{*1}$ . This means that  $b\ 5\Pi_i \rightarrow a\ 5\Sigma^+$  also corresponds to a charge transfer,  $9\sigma \rightarrow 3\pi$ .

## VII. PROPOSED REACTION MECHANISMS

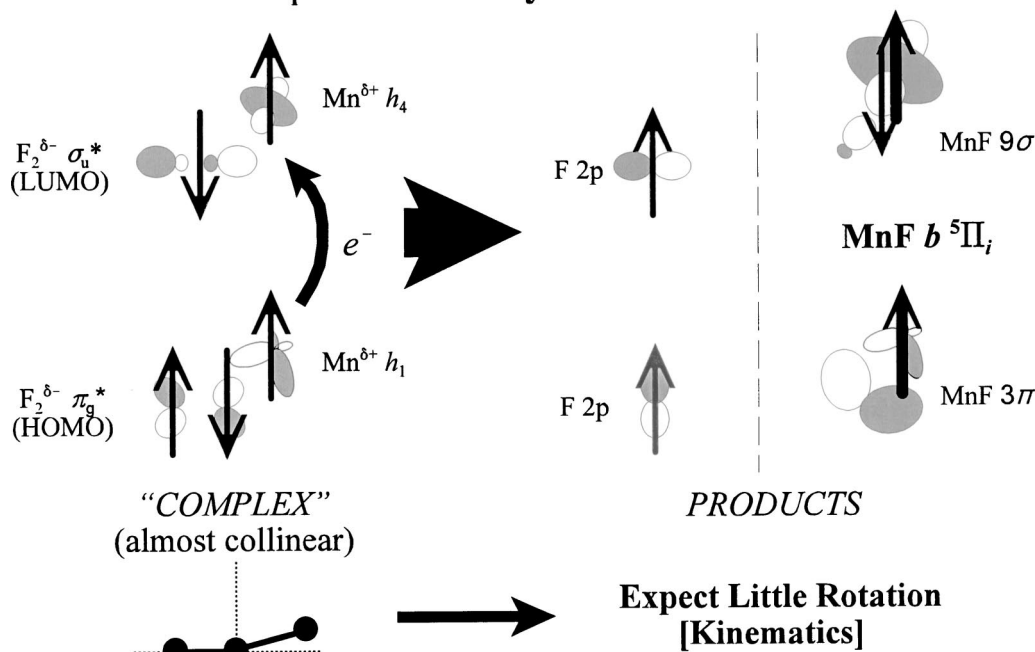
A long-range electron transfer is certainly expected on the basis of Magee's equation for the crossing radius. More importantly, early access to an ionic surface serves to explain the high vibrational excitation that we have found in the  $b$  and  $c$  states, as an early attractive release of the reaction exothermicity should favor vibrational excitation of the product molecule. Note that because the initial electron transfer occurs at long range, energy release is separable—not mixed.

Geometric constraints are not expected to operate at this first crossing from a covalent to an ionic surface in the entrance channel because according to the orbital-locking and-following model,<sup>45,46</sup> orbital steering can occur only when the incoming reagent is close enough to the target reagent so that their orbitals may interact.

From the perspective of the reagent atoms, if the nascent state to be formed is MnF  $b\ 5\Pi_i$ , then the electron will be transferred by  $\sigma$ -forward donation from the  $sd$ -hybrid AO (mostly  $3d_\sigma$ ) of Mn to the  $3\sigma_u^*$  LUMO (—lowest-unoccupied molecular orbital) of  $F_2$  and begin to weaken the F–F bond.  $\pi$  backbonding from fluorine to manganese will further weaken the F–F bond to the point of breaking. The backbonding corresponds to a partial charge transfer from  $F^-$  to  $Mn^+$ , introducing covalent character into the  $b\ 5\Pi_i$  state. (This partial covalent character is why  $b\ 5\Pi_i$  is less ionic than  $a\ 5\Sigma^+$ .) Figure 12 illustrates the orbitals involved in the backbonding that leads to the  $b$  state.

From the perspective of the reagent atoms, if MnF  $c\ 5\Sigma^+$  is to be formed, then the electron will be transferred by

### MnF $b$ $^5\Pi_i$ Formation by $\pi$ -Back-Donation



### MnF $c$ $^5\Sigma^+$ Formation by $\sigma$ -Back-Donation

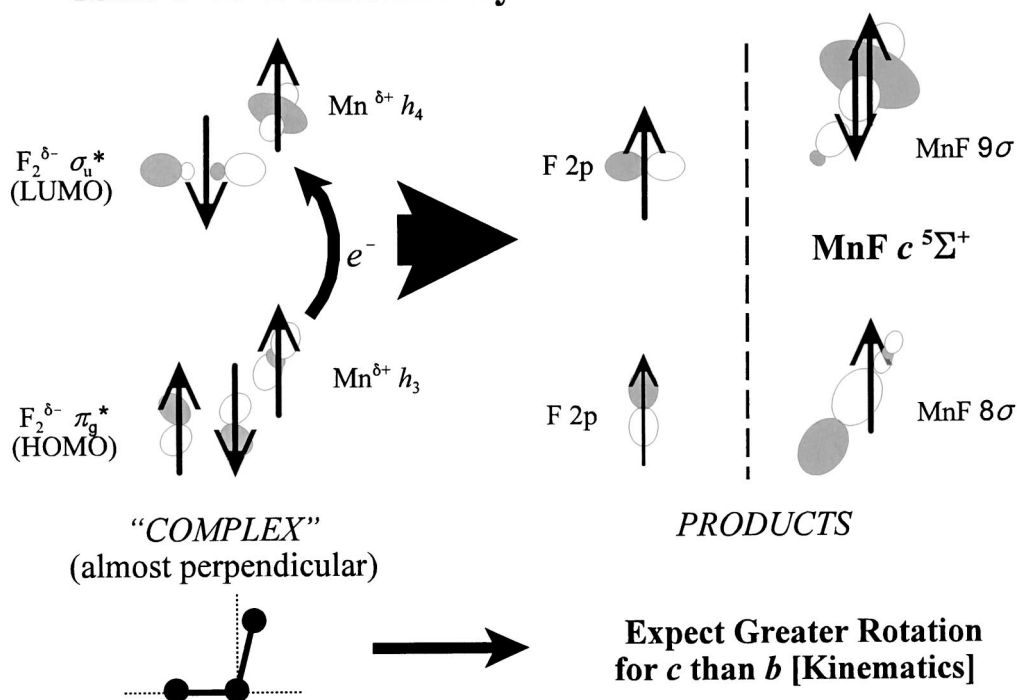


FIG. 12. Backbonding leading to formation of MnF  $b$ ,  $c$ .

$\pi$ -forward donation to the  $3\sigma_u^*$  LUMO of  $F_2$  (the same receiving MO as for the  $b$  state). Then, in this case, it is  $\sigma$  backbonding from the complex that will finally weaken the F–F bond to its breaking point. Figure 12 illustrates the orbitals involved in the backbonding that leads to the  $c$  state.

What might cause the nascent MnF to end up preferentially in the  $b$  or the  $c$  state? Recall that vibrational excitation is usually determined by entrance channel forces while rota-

tional excitation is usually determined by exit channel forces.<sup>47</sup> Consequently, to understand the rotational excitation we need to consider the optimal geometry of interaction of the orbital of the incoming  $Mn^+$  with the  $F_2^- 1\pi_g^*$  HOMO (—highest occupied molecular orbital) that leads to the  $b$  and  $c$  states. While the forward donation is dictated by long-range Coulombic forces and so has no geometric constraints, the backdonation might have geometric constraints. We ex-

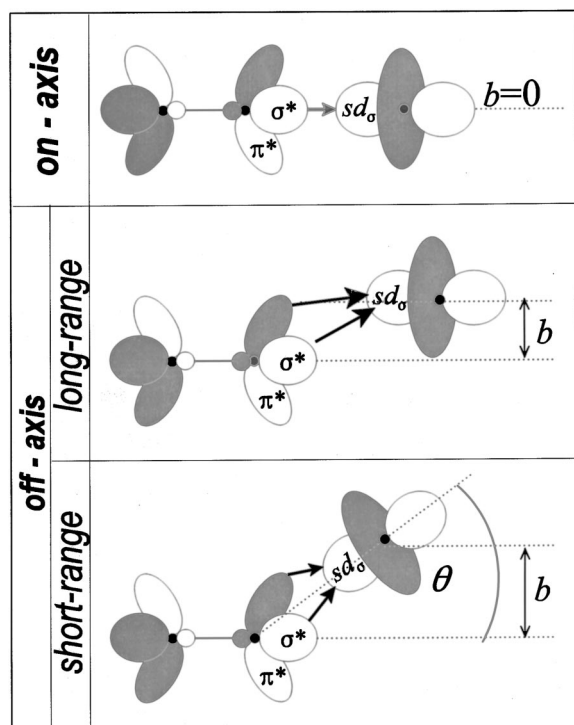


FIG. 13. Orbital interactions of Mn with  $F_2$  at different impact parameters.

amine the geometry of each of the two  $MnF^*$  states of interest ( $b, c$ ) relative to the trajectory of the incoming Mn to the fluorine axis.

At first glance, it appears that off-axis approaches—those approximately orthogonal to the fluorine axis—will favor formation of the  $MnF\ c^5\Sigma^+$  state by optimizing the overlap with the  $Mn^+ h_3$  (mainly,  $3d_{\sigma}$ ) AO and the  $F_2^- 1\pi_g^*$ . Also, at first glance it appears that only an on-axis approach—one collinear with the fluorine axis—will produce the  $b^5\Pi_i$ . One might imagine that the geometry of approach and the impact parameter could specify which  $MnF^*$  state is produced: on-axis collinear  $\Rightarrow b^5\Pi_i$ , and off-axis orthogonal  $\Rightarrow c^5\Sigma^+$ .

A nearly collinear approach (i.e., nearly on-axis approach—one with small impact parameter) is needed to maximize overlap between the incoming  $Mn\ h_1$  (a  $sd_{\sigma}$  hybrid) and the end of the target  $F_2\ 1\pi_g^*$  to produce the  $b^5\Pi_i$ . In contrast, a nearly orthogonal approach (i.e., off-axis approach—one with larger impact parameter) is needed for maximal overlap of the incoming  $Mn\ h_3$  (a  $dp_{\pi}$  hybrid) and the end of the target  $F_2\ 1\pi_g^*$  to produce the  $c^5\Sigma^+$ . So, at first glance, small impact parameters would seem to favor formation of  $b^5\Pi_i$  while larger impact parameters would seem to favor formation of  $c^5\Sigma^+$ .

However, as illustrated in Fig. 13, the off-axis case can actually be subdivided into two cases: (1) orbital steering occurs (adiabatic transition), and (2) no orbital steering occurs (nonadiabatic transition). The adiabatic transition is a discontinuous change in the system's evolution because of orbital steering from the target (controlled by the adiabatic potential), which at onset suddenly reorients the incoming metal's orbitals. This is in direct contrast to the nonadiabatic transition which is a smooth change (controlled by the diaba-

tic potential)—no sudden reorientation of the incoming metal orbital occurs. Hence off-axis reaction could just as easily involve  $\sigma$ -forward donation coupled with  $\pi$  backbonding leading to the  $b$  state, or  $\pi$ -forward donation coupled with  $\sigma$  backbonding leading to the  $c$  state.

This description using qualitative MO's suggests that the ionic and covalent potential surfaces should have a conical intersection for the collinear configuration. Passage through the conical intersection from ionic to covalent surfaces would lead exclusively to the  $b$  state, whereas off-axis switching of surfaces can proceed adiabatically to either the  $b$  or  $c$  state.

However, if locking and steering of  $Mn^+$  orbitals to the incipient  $Mn^+ - F^-$  axis takes place after the initial electron transfer, there may be a propensity for  $\sigma$  backbonding because it is difficult to imagine how a  $\pi$ -type interaction could serve to define the  $Mn - F$  axis as effectively as a  $\sigma$ -type interaction could.

Both of these considerations suggest that more nearly collinear collisions with smaller impact parameters favor formation of the  $b$  state. Such collisions should lead to lower  $MnF$  rotational excitation for two reasons: less angular momentum is available to be shared by product orbital and rotational angular momenta, and less torque can be exerted on  $MnF$  as it is pushed away from  $F$  in a near-collinear geometry. This may explain why a smaller fraction of energy available is observed to go into rotational energy of  $b^5\Pi_i$  vs  $c^5\Sigma^+$ .

To summarize, it is not only the geometry of approach and the impact parameter that determine which state is produced—the relative speed of the incoming target also plays a role in determining if the reaction will follow the adiabatic or diabatic potential surface. Our proposed mechanism exhibits dynamic control—the course of the reaction is determined both by geometric factors and by dynamic factors. Note that we are not concerned here with the absolute  $b/c$  ratio, which was not determined in our experiments. Rather, attention has been directed toward whether the geometry of the transient intermediate can be related to preferential formation of one state or the other. The major role that dynamics plays in these reactions may be contrasted with our earlier conclusions on the  $Mn + O_3 \rightarrow MnO^* + O_2$  reaction, which were that energy disposal was largely kinematically controlled. Perhaps the difference originates in the way that ionic forces in the  $MnF$  reactions can better serve to separate energy release in the entrance and exit channels.

## VIII. CONCLUSIONS

We have investigated the elementary chemiluminescent reaction of Mn with  $F_2$  using the molecular beam technique. The observed spectra due to the  $c^5\Sigma^+ \rightarrow a^5\Sigma^+$  and  $b^5\Pi_i \rightarrow a^5\Sigma^+$  transitions were fit by varying the vibrational and rotational populations in the  $b$  and  $c$  states. Significant vibrational excitation was found for both states, but the rotational excitation was less than the prior expectations, particularly for the  $b$  state. The likely cause for vibrational excitation is a common ionic intermediate for these two exit channels.

For MnF  $b^5\Pi_i$ , the initial bonding comes from the  $\sigma$ -forward donation from Mn into the  $3\sigma_u^*$  MO of  $F_2^-$ . Then  $\pi$  backdonation takes place from the  $1\pi_g^*$  MO of  $F_2^-$ , filling the  $9\sigma$  MO of MnF, but leaving the  $3\pi$  MO with a vacancy. The  $b$  state can be generated from both on-axis diabatic and off-axis adiabatic potential surfaces. Products generated through the diabatic pathway are expected to be rotationally colder than those produced via the adiabatic pathway.

For MnF  $c^5\Sigma^+$ , the initial bonding comes from  $\pi$ -forward donation from Mn into the  $3\sigma_u^*$  MO of  $F_2^-$ . The bonding is strengthened by  $\sigma$  backdonation from the  $1\pi_g^*$  MO, again filling the  $9\sigma$  MO of MnF, but leaving the  $8\sigma$  MO with a vacancy. Intermediate configurations close to collinear are not expected to yield MnF  $c^5\Sigma^+$ , and so some rotational angular momentum might be generated as the F atom recedes from the MnF product.

- <sup>1</sup>J. L. Gole and T. C. Devore, J. Phys. Chem. **100**, 5660 (1996).
- <sup>2</sup>R. P. Kampf, Ph.D. thesis, The Ohio State University, 1999.
- <sup>3</sup>K. P. Hüber and G. Herzberg, *Molecular Spectra and Molecular Structure. IV. Constants of Diatomic Molecules* (Van Nostrand Reinhold, New York, 1979).
- <sup>4</sup>W. Hayes and T. E. Nevin, Proc. Phys. Soc. London **68**, 665 (1955).
- <sup>5</sup>W. Hayes, Proc. Phys. Soc. London **68**, 1097 (1955).
- <sup>6</sup>R. P. Hayes and T. E. Nevin, Nuovo Cimento, Suppl. **2**, 734 (1955).
- <sup>7</sup>O. Launila and B. Simard, J. Mol. Spectrosc. **154**, 407 (1992).
- <sup>8</sup>O. Launila and B. Simard, J. Mol. Spectrosc. **154**, 93 (1992).
- <sup>9</sup>B. Simard and O. Launila, J. Mol. Spectrosc. **168**, 567 (1994).
- <sup>10</sup>O. Launila, B. Simard, and A. M. James, J. Mol. Spectrosc. **159**, 161 (1993).
- <sup>11</sup>B.-S. Cheong, M. D. Oberlander, R. P. Kampf, and J. M. Parson, J. Chem. Phys. **99**, 5104 (1993).
- <sup>12</sup>K. M. Green, M.S. thesis, The Ohio State University, 1999.
- <sup>13</sup>W. E. Blass, Appl. Spectrosc. Rev. **11**, 57 (1976).
- <sup>14</sup>P. Pelikán, M. Ceppan, and M. Liška, *Applications of Numerical Methods in Molecular Spectroscopy* (CRC, Boca Raton, FL, 1993), Chap. 1.
- <sup>15</sup>K. M. Green, Ph.D. thesis, The Ohio State University, 2002.
- <sup>16</sup>D. S. Sivia, *Data Analysis: A Bayesian Tutorial* (Oxford University, New York, 1996).
- <sup>17</sup>W. H. Breckenridge, J. Phys. Chem. **100**, 14840 (1996).
- <sup>18</sup>D. K. Liu, Y. R. Ou, and K. C. Lin, J. Chem. Phys. **104**, 1370 (1996).
- <sup>19</sup>T. H. Wong, C. Freel, P. D. Kleiber, and K. M. Sando, J. Chem. Phys. **108**, 5723 (1998).
- <sup>20</sup>M. Roth, C. Maul, and K.-H. Gericke, J. Chem. Phys. **107**, 10582 (1997).
- <sup>21</sup>D. Xie, H. Guo, Y. Amatatsu, and R. Kosloff, J. Phys. Chem. A **104**, 1009 (2000).
- <sup>22</sup>J. P. Reid, R. A. Loomis, and S. R. Leone, Chem. Phys. Lett. **324**, 240 (2000).
- <sup>23</sup>A. Burroughs and M. C. Heaven, J. Chem. Phys. **114**, 7027 (2001).
- <sup>24</sup>I. Kovács, *Spectra of Diatomic Molecules* (American Elsevier, New York, 1969).
- <sup>25</sup>E. E. Whiting, J. A. Paterson, I. Kovács, and R. W. Nicholls, J. Mol. Spectrosc. **47**, 84 (1973).
- <sup>26</sup>U. Sassenberg, A. S.-C. Cheung, and A. J. Merer, Can. J. Phys. **62**, 1610 (1984).
- <sup>27</sup>I. Kovács, J. Mol. Spectrosc. **98**, 41 (1983).
- <sup>28</sup>I. Kovács, J. Mol. Spectrosc. **126**, 140 (1987).
- <sup>29</sup>I. Kovács and J. Antal, Can. J. Phys. **62**, 1603 (1984).
- <sup>30</sup>P. F. Bernath, *Spectra of Atoms and Molecules* (Oxford University, New York, 1995).
- <sup>31</sup>R. N. Zare, *Angular Momentum: Understanding Spatial Aspects in Chemistry and Physics* (Wiley-Interscience, New York, 1988).
- <sup>32</sup>V. D. Kleiman, H. Park, R. J. Gordon, and R. N. Zare, *Companion to Angular Momentum* (Wiley, New York, 1998).
- <sup>33</sup>J. T. Hougen, *The Calculation of Rotational Energy Levels and Rotational Line Intensities in Diatomic Molecules*, Nat. Bur. Stand. (U.S.) Circ. No. 115 (U.S. GPO, Washington, D.C., 1970).
- <sup>34</sup>J. L. Magee, J. Chem. Phys. **8**, 687 (1940).
- <sup>35</sup>M. Dolg, U. Wedig, H. Stoll, and H. Preuss, J. Chem. Phys. **86**, 866 (1987).
- <sup>36</sup>C. E. Moore, *Atomic Energy Levels as Derived from the Analyses of Optical Spectra*, Nat. Bur. Stand. (U.S.) Circ. No. 467 (U.S. GPO, Washington, D.C., 1952).
- <sup>37</sup>P. G. Wenthold and R. R. Squires, J. Phys. Chem. **99**, 2002 (1995).
- <sup>38</sup>K. M. Green, R. P. Kampf, and J. M. Parson, J. Chem. Phys. **112**, 1721 (2000).
- <sup>39</sup>M. Bencheikh, J. Mol. Spectrosc. **183**, 419 (1997).
- <sup>40</sup>Y. Jean, F. Volatron, and J. Burdett, *An Introduction to Molecular Orbitals* (Oxford University, New York, 1993).
- <sup>41</sup>T. A. Albright and J. K. Burdett, *Problems in Molecular Orbital Theory* (Oxford University, New York, 1992).
- <sup>42</sup>F. Mathey and A. Sevin, *Molecular Chemistry of the Transition Elements: An Introductory Course* (Wiley, New York, 1996).
- <sup>43</sup>R. Koivisto, O. Launila, B. Schimmelpfennig, B. Simard, and U. Wahlgren, J. Chem. Phys. **114**, 8855 (2001).
- <sup>44</sup>J. F. Harrison and J. H. Hutchison, Mol. Phys. **97**, 1009 (1999).
- <sup>45</sup>E. E. B. Campbell, H. Schmidt, and I. V. Hertel, Adv. Chem. Phys. **72**, 37 (1988).
- <sup>46</sup>I. V. Hertel, H. Schmidt, A. Baehring, and E. Meyer, Rep. Prog. Phys. **48**, 375 (1985).
- <sup>47</sup>B. Bourguignon, M. A. Gargoura, J. Rostas, and G. Taieb, J. Phys. Chem. **91**, 2080 (1987).
- <sup>48</sup>W. J. Balfour, O. Launila, and L. Klynning, Mol. Phys. **69**, 443 (1990).
- <sup>49</sup>A. S.-C. Cheung, W. Zyrnicki, and A. J. Merer, J. Mol. Spectrosc. **104**, 315 (1984).
- <sup>50</sup>J. M. Brown and D. J. Milton, J. Mol. Phys. **31**, 409 (1976).
- <sup>51</sup>R. A. Kent, T. C. Ehlert, and J. L. Margrave, J. Am. Chem. Soc. **86**, 5090 (1964).